EFFICIENT CLUSTER IDENTIFICATION FOR MEASURED ULTRA-WIDEBAND CHANNEL IMPULSE RESPONSE IN VEHICLE CABIN

B. Li [*], Z. Zhou, D. Li, and S. Zhai

Key Lab of Universal Wireless Communications, Ministry of Education (MOE), Beijing University of Posts and Telecommunications (BUPT), China

Abstract—Although automatic and robust cluster identification is crucial for ultra-wideband propagation modeling, the existing schemes may either require interactions with analyst, or fail to produce reasonable clustering results in more universal propagation environments. In this article, we suggest a novel cluster identification algorithm. Rather than assuming the limited exponential power decay characteristics on UWB channels, from a novel perspective cluster identification is formulated as the local discontinuity detection based on wavelet analysis. Firstly, in order to comprehensively reflect the prevailing amplitude changes induced by new clusters, the moving averaging ratio is extracted from the measured UWB channel impulse responses. Subsequently, the appealing local-transient analysis ability of wavelet transform is properly exploited, and a computationally efficient cluster extraction method is developed. Distinguished from the subjective visual inspection and excluding any analyst interaction, the presented scheme can automatically discover multiple clusters. Our algorithm is premised on the general amplitude discontinuity and hence is applicable to various complicated operation environments. Moreover, the produced clustering results, essentially depicting realistic physical propagations, are basically independent of parameter configurations. Experiments on both simulated channels and the measured data in typical vehicle cabin validate the proposed method.

1. INTRODUCTION

The growing interests in ultra-wideband (UWB) are stimulated by both the significant military applications, such as UWB radars and high-resolution positioning [1, 2], and the promising commercial applications, such as high speed transmissions in wireless personal area networks (WPANs) [3] and low-power wireless sensor networks (WSNs) [4]. In essence, the extremely large bandwidth ($> 500\,\mathrm{MHz}$) leads to the appealing characteristics of UWB systems, including the fine temporal resolution, immune to multipath fading, high transmission capacity and extremely low power emission [1, 5, 6].

Due to excellent time resolution typically on a nanosecond (ns) scale, UWB propagations remarkably differ from traditional narrowband channels. The intensive multipath components (MPCs) can be observed in measured UWB channels [7–9]. The resolvable trajectories, which are reflected from different large objects in operation environments, (e.g., walls and desks), usually arrive in a discontinuous manner, i.e., grouped into several distinguishing clusters [8, 9]. This tendency was originally reported by the well-known Saleh-Valenzuela (S-V) indoor channel modeling [10]. Lately, a modified S-V model was adopted by the IEEE 802.15.3a and 802.15.4a WPAN task groups (TGs) for UWB propagations [11, 12].

Intending for fair comparison of physical (PHY) and media access control (MAC) designing, the works in [11] and [12] have contributed greatly to the understanding of the nature and structure of UWB channel impulse responses (CIRs). However, there still exists an ongoing need to analyze and model the detailed structure of UWB CIRs, which usually plays a significant role in design signaling scheme and receiver architecture [6, 9]. Practically, cluster identification of CIRs is much crucial for UWB research. First, cluster identification is of great importance to channel modeling, since cluster extraction serves as a basis for parameters extraction of S-V channel. Second, clustering property can be properly exploited in receiver designing, for example in channel estimation [13], low-complexity detector [14] and synchronization [15]. Unfortunately, most current literatures still identify cluster through the time-consuming "visual inspection" technique [9, 16]. Such a method significantly relies upon *subjective* assessments of analysts, which on one hand is considerably susceptible to inconsistency for different observers, and on the other hand, becomes impractical for a large amount of measurement data, hence preventing us from drawing more profound conclusions on UWB propagations.

Recently, a computer-assisted cluster identification scheme is proposed in [17, 18]. By exploiting the exponential decay profile of

cluster power and the multivariate adaptive regression spline technique (MARS), the least-squares (LS) linear regression is utilized to provide a *user-interactive* solution to identify clusters, in a relatively objective manner [18]. This method iteratively discovers possible clusters that best fit UWB CIRs, until a pre-specified minimum square error (MSE) between the extracted clusters and UWB channel is fulfilled. Nevertheless, this cluster extraction scheme can only be applied to some special line-of-sight (LOS) environments where each cluster strictly follows an exponential decay rule. Hence, the generality of this algorithm cannot be guaranteed. Besides, the computational complexity of the intensive *trial* searching is also impractical. More importantly, the scheme involves many parameters, such as MSE threshold and a prior MPC interval [18], which should be interactively determined by analyst to obtain a reasonable clustering result. Due to this assisted essence, it still cannot be applied automatic data analysis. Additionally, this mathematical fitting inspired cluster identification may ignore the nature of physical propagations, and sometimes may produce numerous clusters by misunderstanding local amplitude discontinuity aroused by small-scale fading [17].

Motivated by the considerations above and relying on our recent UWB channel measurement campaign, an efficient cluster identification algorithm based on wavelet analysis is presented in this paper. After data pre-processing, i.e., antenna calibration and deconvolution [8, 9], the discrete UWB CIRs are extracted from the frequency-domain measurements. Subsequently, a novel moving averaging ratio (MAR) is used to reinforce the amplitude discontinuity in UWB CIRs. The powerful local-transient analysis ability of continuous wavelet transform (CWT) is then exploited. Finally, the local breakpoints/discontinuities in MAR signal, indicating the possible cluster locations, are accurately discovered in parallel. This suggested algorithm is basically premised on the physical nature of UWB propagations, e.g., the general amplitude discontinuity introduced by different clusters. Hence, it can identify clusters in UWB CIRs automatically without any assistance from analysts, which also shows remarkable robustness to parameter configurations. Strikingly in contrast to the other existing schemes, e.g., linear-regression technique, even if the intercluster MPCs does not follow exponential decay as is in complicated operation environments, (e.g., the measured vehicle cabin), this algorithm can still efficiently discover multiple clusters. Further taking its efficient computation into consideration, our presented algorithm may provide an appealing framework for cluster identification, which can significantly facilitate a large amount of data analysis and further give us a more comprehensive

understanding to UWB propagations.

The rest of this paper is structured as following. The classical S-V channel modeling is briefly introduced in Section 2. Then, the frequency-domain UWB propagations measurement is depicted in Section 3, accompanying the data pre-processing by which discrete CIRs can be extracted. Subsequently, a new cluster identification algorithm based on wavelet analysis is developed in Section 4. Experiments on both the measured propagations and simulated CIRs are presented in Section 5. Finally, we conclude the whole work in Section 6.

2. UWB CHANNEL MODELING

Attributed to the excellent temporal resolution of transmitted short pulses and the rich scatters in typical indoor environments, the short-range UWB channel is known to be linearly dispersive with tens or hundreds of resolved MPCs [8, 9]. Based on the modified S-V channel modeling, the IEEE 802.15.3a TG defines several channel types for UWB applications in dense multipath environments [11]. The unified time domain expression of UWB CIRs can be expressed as

$$h(t) = X \sum_{l=0}^{L-1} \sum_{k=0}^{K-1} \alpha_{k,l} \delta\left(t - T_l - \tau_{k,l}\right) \qquad (1)$$

where L is the number of clusters, K is the number of rays of each cluster, $\alpha_{k,l}$ is the fading coefficient of the kth path of the lth cluster, X is the channel fading factor, T_l is the arrival time of the l cluster and $\tau_{k,l}$ is the delay of the kth path of the lth cluster relative to T_l. T_l and $\tau_{k,l}$ has a Poisson distribution, $\alpha_{k,l}$ and X are log-normal random variables [11].

After the small-scale fading has been suppressed, the power delay profile (PDP) can be well described by the product of two exponential functions [9, 16].

$$E\left\{|a_{k,l}|^2\right\} \propto \exp\left(-T_l/\Gamma\right) \exp\left(-\tau_{k,l}/\gamma\right) \qquad (2)$$

where Γ and γ denote the cluster and intercluster decay constants, respectively [9, 11]. Notice that, many measurements also reveal that the UWB PDP shape may not be strictly monotonic, but exhibit a *soft-onset* shape in non-line-of-sight cases (NLOS) [16]. Specially, the cluster PDP increases firstly until a local maximum, and then shows decease. Hence, the following PDP has been suggested to depict the observed phenomenon.

$$E\left\{|a_{k,l}|^2\right\} \propto \left(1 - \chi \exp\left(-\tau_{k,l}/\gamma_{rise}\right)\right) \exp\left(-\tau_{k,l}/\gamma_1\right) \qquad (3)$$

where χ denotes the attenuation of the first component, γ_{rise} determines how fast the PDP rises to its local maximum, and γ_1 represents the decay at later times.

3. UWB CHANNEL MEASUREMENT

Many experiments on channel measurement have been reported since the birth of the first literature on UWB propagations [7, 8, 18–20]. To deepen our understanding of UWB propagations, as is suggested by [16, 18], many experimental works are still needed currently. Meanwhile, it is also noted that few existing works on experiment measurement can occupy all the whole authorized UWB bands, i.e., 3.1–10.6 GHz. Recently, we launched a new UWB measurement campaign in frequency-domain by using a much wider sweeping bandwidth of 8.7 GHz, i.e., 2.3–11 GHz, which considerably helps us draw some more profound conclusions on UWB propagations. Moreover, by using the frequency-domain windowing technique on measured data, our research can also easily cover the prevailing working band of 6–9 GHz with a worldwide overlap [21], which may hence provide more practical instructions for UWB product designing.

3.1. Measurements

UWB channel measurements aim to determine the realistic CIRs. In our experiments, the popular frequency-domain technique by using a vector network analyzer (VNA) is adopted, which measures the transfer function by exciting the channel with slowly frequency-sweeping sinusoidal waveform [16]. A typical setup for frequency-domain measurement has been illustrated in Figure 1(a), the channel sounder mainly consists of the *Agilent N5269 VNA*, which sweeps the frequency response from 2.3 GHz to 11 GHz in 5600 linearly distributed points, i.e., the frequency sweeping interval is about 1.55 MHz.

Our measurements have been conducted in residential, commercial and industrial environments. In this investigation, however, we mainly focus on measured data from vehicle passenger cabin. The UWB propagation in typical vehicle environments involves numerous reflections, i.e., passenger seats and walls, by which the efficient clusters identification algorithm can be developed and tested. As is shown in Figure 1(b), the measured vehicle is 10.4 m long and 2.5 m wide, having 50 passenger seats. The distance from ceiling to floor is about 2 m. The vehicle walls are made of metallic materials. The topology is shown in Figure 1(c), in which the measurement equipments deployment is illustrated. Two omni-directional UWB antennas working in 2.3 GHz–
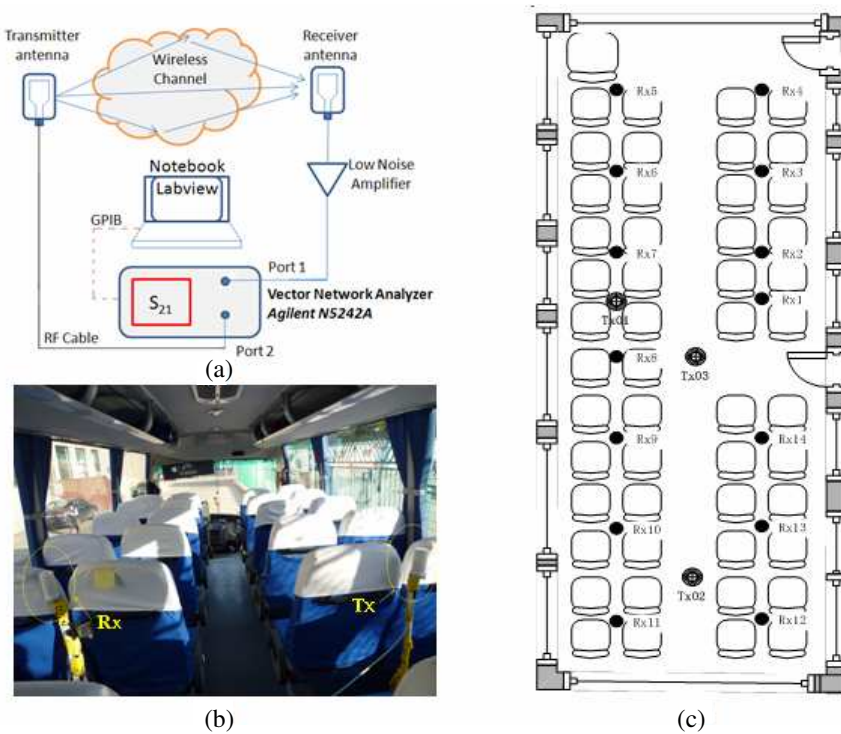
Figure 1. (a) Typical setup for the frequency-domain measurement. (b) The testing scene in vehicle cabin. (c) The topology of vehicle cabin and measurement antennas deployment.

11 GHz are used, whose amplitude frequency response (AFR) is given in Figure 2(a). In fact, remarkable advances have been made in UWB antenna designing within the past few years. The main stream technologies include monopole antenna [22–24], slot antenna [25–28] and printed antenna [29, 30]. In experiment, UWB planar antenna is based on the popular *triangular monopole* design technology [31–33], with the voltage standing wave ratio (VSWR) less than 2.25 across the working band. The azimuth gain variation (AGV) is about $\pm 1.25\,\text{dB}$, and the dimension is $50 \times 20 \times 20\,\text{mm}^3$. The measured transfer function of UWB propagation is shown in Figure 2(b).

3.2. Pre-processing

After obtaining the frequency-domain measured data, we have to perform data pre-processing to further extract the discrete UWB
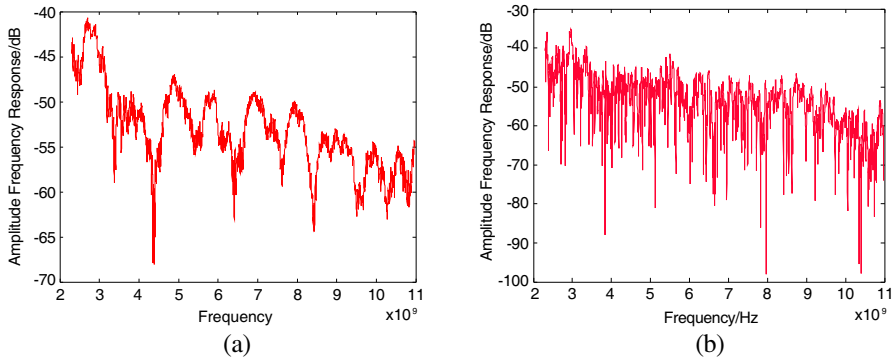
Figure 2. (a) Amplitude frequency response $A(f)$ of the omni-directional UWB antennas. (b) The amplitude of measured UWB channel transfer function, i.e., $S(f)$.

CIRs. Usually, this process mainly includes two steps, that is, antenna calibration and time-domain deconvolution [9, 16].

Notice that, the frequency response of radio frequency (RF) cable connecting the transmitter antenna (or receiver antenna) and VNA can be conveniently compensated by VNA itself. Thus, the antenna response may have a significant impact on the measurement results. On one hand, the *non-flat* antenna AFR will attenuate the arriving signals, and on the other hand, the directional pattern weights the MPCs arriving from different directions, introducing remarkable distortion on measured data [9, 16]. In our experiment, however, the direction-independent UWB antennas are used, and hence the directional distortion can be reasonably ignored. Hence, only the antenna frequency response shown in Figure 2(a) should be calibrated. Specifically, denote the antenna frequency response by $A(f)\exp[-j2\pi\theta_a(f)]$, where $A(f)$ is amplitude response and $\theta_a(f)$ accounts for antenna phase response, and the measured frequency-domain data by $S(f)\exp[-j2\pi\theta_s(f)]$, where $S(f)$ is Fourier transform of UWB CIRs and $\theta_s(f)$ is the corresponding phase response. Then, the calibrated transfer function $S_c(f)$ can be given by:

$$S_c(f) = S(f)/A(f)\exp\left[-j2\pi\left(\theta_s(f) - \theta_a(f)\right)\right] \qquad (4)$$

Additionally, in order to extract the measured data of interest, a windowing process is usually applied to specified frequency band $[f_1, f_2]$. In our analysis, we set $f_1 = 6\,\text{GHz}$ and $f_2 = 9\,\text{GHz}$, and a Gaussian windowing is used in transition bands, as shown in Figure 3(a). Then, the time-domain UWB CIR can be obtained after inverse discrete
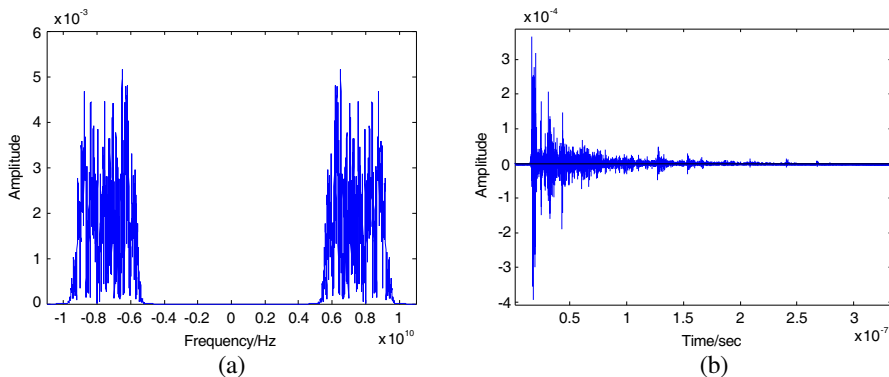
Figure 3. (a) Measured transfer function in [6 9] GHz without antenna calibration. Notice that, a conjugate symmetric spectrum has been constructed. (b) The extracted discrete UWB CIR after windowing, antenna calibration and time-domain deconvolution.

Fourier transform (IDFT) has been performed on the windowed data, i.e., $h(t) = \text{IDFT}\ (S_c(f))$. Subsequently, a deconvolution process is necessary in order to extract the discrete CIR $h(n)$ [9]. Usually, the well-known CLEAN algorithm is used to perform this function [16]. The CLEAN method is generally a serial-interference cancellation algorithm (SIC). The basic premise is that, the observed signal is a sum of pulse with known shape $p(t)$ [34]. It first finds the largest pulse by determining the correlation of received signal with $p(t)$, and identifies the highest peak. This discovered pulse is then subtracted from the total signal, and hence the pulse is correlated with the clear-up signal. This process is repeated until the energy of cleaned-up signal falls below a threshold [9, 34]. Notice that, the pulse shape $p(t)$ can be numerically derived, given the adopted windowing function and frequency band.

In our experiment, the stopping threshold is set to 0.1% of the maximum MPC. After antenna calibration, windowing and deconvolution, one of the recovered discrete UWB CIR has been shown in Figure 3(b). In order to evaluate the accuracy of deconvolution process, we further convolute this discrete CIR with the used pulse shape, and the MSE between reconstructed signal and $h(t)$ is 3%, i.e., with a energy capture ratio of 97%. So, the recovered CIRs can be regarded as an accurate discrete representation of measured UWB channels.

4. CLUSTER IDENTIFICATION

For the issue of cluster identification in UWB CIRs, firstly a crucial question is that how we can reasonably define a cluster. Although it is widely recognized that clusters are groups of MPCs having similar *larger-scale* property, such as time of arrival (ToA), angle of arrival (AoA) and amplitude decay [20, 35, 36], there still is a surprising lack of agreement concerning of a cluster definition. In [37], ToA is assumed to be a hidden Markova modeling (HMM), based on which cluster identification for S-V channel is realized. However, by ignoring amplitude discontinuity the recovered clusters overlap with each other, in which channel response is also impractically supposed to be *sparse* [37]. Hence, although significant theoretical contributions, this cluster identification can be hardly applied to UWB channel modeling and practical system designing, e.g., the PDP weighted noncoherent detector [14]. Assuming that different clusters with exponential PDP introduce remarkable amplitude discontinuity, Ref. [17] uses a piecewise linear regression to identify involved clusters. Nevertheless, this mathematical trial-fitting technique consumes much computation resources, and also requires the aid from analyst to develop a reasonable result, making it impractical for automatic data analysis. More importantly, for the more general soft-onset PDP [15], this method may even fail due to the obscure breakpoints in measured CIRs.

In order to develop an efficient cluster identification algorithm, two practical difficulties must be taken into considerations. First, due to specula reflections or shadowing effects, many UWB measurements
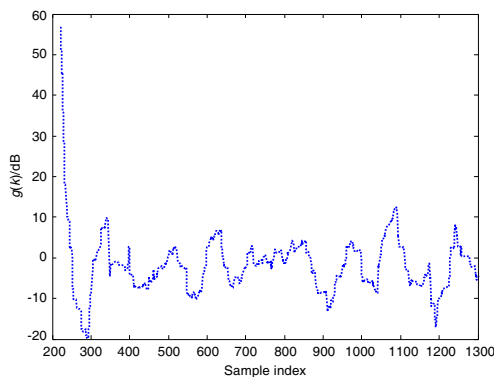

Figure 4. The obtained MAR signal with an averaging length M of 50.

have shown strong components for later clusters or the soft-onset phenomenon [16, 20]. Hence, the search algorithm should identify exact cluster *start-points* rather than local maximums, by ensuring the intercluster MPCs having similar property. Second, as is suggested by the IEEE 802.11n TG [38], a cluster may begin and even continue indefinitely. Although the overlapped MPCs fallen into subsequent clusters do not affect the new breakpoints, identifying these small MPCs may become a rather *ambiguous* procedure, which also has no reward in system designing [14]. In fact, these overlapped small MPCs may even be added to new arrived clusters.

As the cluster start-points are essentially significant to both channel parameters extraction and system designing, we establish an appealing cluster identification method based on the discontinuity detection. It should be stressed that, following our discussions above, the breakpoints to be detected should explain the *overall* MPCs tendency, rather than the *single* MPC amplitude singularity [16, 17]. The philosophy behind is rather straightforward. That is, irrespective of small-scale fading, the cluster group generated from a large reflection object should be noticeably distinguished from the former clusters reflected from other different objects [9]. Our cluster identification technique mainly involves two steps. A moving average ratio (MAR) of UWB CIRs is firstly suggested to exploit such local discontinuity property, and then, wavelet analysis is applied to the MAR signal, which further identifies multiple clusters of UWB CIRs in parallel.

4.1. Moving Averaging Ratio

As is well known, moving average (MA) operations have found broad applications in voice signal processing [39], which can efficiently suppress temporal changes (small-scale fading) and also enhance long-term characteristic of a signal. Nevertheless, as a low-pass filter, unfortunately this process may also smooth local breakpoints, leading to the failure of discontinuity detection. In this cluster identification problem, we further suggest a novel MAR to suppress the small-scale effects, and simultaneously preserve the overall singularity of UWB CIRs. Assume the extracted discrete CIR is denoted by $h(n)$ and MAR by $s(k)$, we have:

$$s(k) = \sum_{i=k}^{i=k+M-1} h^2(i) \Big/ \sum_{i=k-M}^{i=k-1} h^2(i), \ k = M, M+1, \ldots, N-1-M \quad (5)$$

Here, N is the length of the discrete CIR $h(n)$, while M denotes the average length. For $k = 0, 1, 2, \ldots, M-1$, we set $s(k) = 1$. In practice, the selection of M may have some impact on subsequent

processing, which will be elaborated in Section 4.4. Due to arrival of strong signals in the first cluster, it is obvious that the first breakpoint is dramatically larger than the other ones. In order to minimize the discontinuity difference and facilitate subsequent cluster identification, we further perform the logarithmic transform on $s(k)$, then we have $g(k) = 10 \times \log(s(k))$. The obtained MAR signal $g(k)$ is also illustrated in Figure 4 with $M = 50$.

We can note that there indeed exist many pronounced local rises (or discontinuities) in $g(k)$. Usually, these local-transients are aroused by the soft-onset property of UWB CIRs. This may considerably differs from the first cluster in LOS case, where strong MPCs appear in the near beginning, and a sharp amplitude change can be observed. The breakpoints in $g(k)$, exhibiting noticeable amplitude jump, are essentially related with successive MPCs groups, which have experienced different reflections before arriving.

Apparently the discontinuity areas give us an initial estimation of cluster locations. Nevertheless, there are two considerations remained in the local-discontinuity inspired cluster identification. First, although the discontinuities are relatively conspicuous from visual inspection, exact breakpoints still cannot be discovered automatically, as there is a lack of quantifiable criterion of singularities. Second, there exist many small-region rises in $g(k)$, which are mainly caused by random noise. Hence, the efficient cluster identification should cautiously find realistic clusters, while exclude *fake* clusters aroused by noise or specula reflections.

4.2. Wavelet Analysis

4.2.1. Wavelet Analysis

Following the elaborations above, the problem of cluster identification can be transformed into searching local amplitude transients in the developed MAR, which is also known to be discontinuity or singularity detection [40]. It has been shown that analyzing a signal at different *scales* may considerably increase the accuracy and reliability of discontinuity detection [41]. As is well known, wavelet analysis is capable of revealing data characteristics such as trends, breakdown points and self-similarity, which may be usually missed by other signal analysis techniques. One major advantage afforded by wavelet analysis is the ability to analyze a localized area of input signal. Focusing on signal's local-transient behaviors, with a zooming procedure enables simultaneous analysis from a rough to a fine shape. Attributed to this powerful ability, wavelet transform has been widely adopted to perform edge detection in different applications [42–44], which can be

also properly used to detect local breakpoint in MAR signal and hence realize cluster identification.

In general, wavelets are characterized by scale α and position τ, where the parameter α scales the wavelet function by compressing or stretching it, while τ brings a translation on wavelet function along time axis. Consequently, wavelet transform can focus on localized signal structures with a zooming procedure, which progressively reduces the scale parameter α. In such a way, both rough and fine signal structures can be simultaneously analyzed at different scales, which is of great significance to realistic discontinuity detections. Wavelet transform of the MAR signal $g(k)$ can be expressed as [45]:

$$W_g(\alpha, \tau) = \sum_{n=0}^{N-M} \frac{1}{\sqrt{\alpha}} g(n) \psi \left(\frac{n - \tau}{\alpha} \right) \tag{6}$$

where $\psi(t)$ is referred to as the mother wavelet, which serves as a prototype wavelet from which all other wavelets can be generated. A scaling function $\phi(t)$ is usually associated with wavelet function $\psi(t)$, and the elegant wavelet analysis framework can be established by combining them together [45–47]. Usually, they should satisfy the following conditions:

$$\int_{-\infty}^{+\infty} \psi(t)dt = 0, \quad \int_{-\infty}^{+\infty} |\psi(t)|^2 \, dt = 1 \tag{7}$$

$$\int_{-\infty}^{+\infty} \phi(t)dt = 1, \quad \int_{-\infty}^{+\infty} |\phi(t)|^2 \, dt = 1 \tag{8}$$

4.2.2. Daubechies Wavelets

In practice, the selection of mother wavelet depends on the properties of local signal structures to be detected. In our analysis, the Daubechies wavelet is adopted [45], whose advantages in discontinuity detection will be elaborated shortly. According to the *multi-resolution analysis* (MRA) theory [48], we may have

$$\phi(t) = \sum_{k \in Z} c_k \sqrt{2} \phi(2t - k) \tag{9}$$

for a group coefficients $\{c_k\}$, and Z denotes a set of integers $[0, 1, \ldots, N - 1]$. A wavelet $\psi(t)$ can be then defined by:

$$\psi(t) = \sum_{k \in Z} (-1)^k c_{1-k} \sqrt{2} \phi(2t - k) \tag{10}$$

The orthogonality of $\phi(t)$ and $\psi(t)$ also leads to [45]:
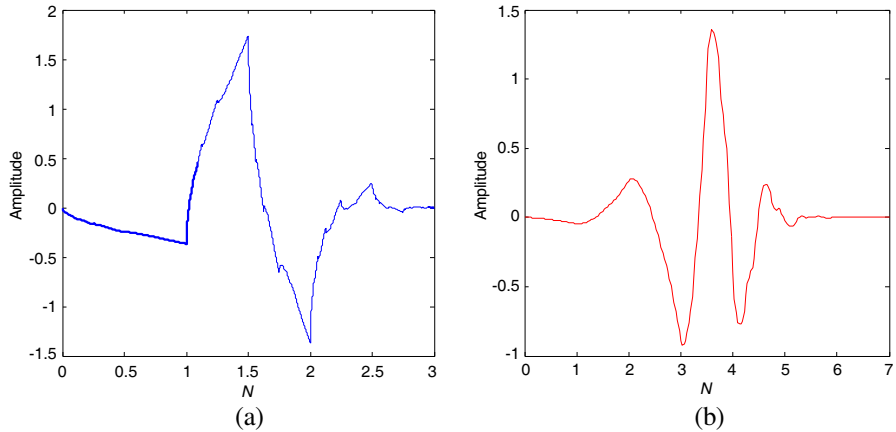
$$\sum_{k \in Z} (-1)^k c_k c_{1-k} = 0 \tag{11}$$

Figure 5. Daubechies wavelet functions. (a) The 2nd order Daubechies wavelet, $n = 10$; and (b) the 4th order Daubechies wavelet, $n = 5$.

In order to obtain the wavelet bases that provide considerably powerful local analysis ability, for the Daubechies wavelet, the high-order moments are supposed to be equal to zero [45, 49]

$$\int_{-\infty}^{+\infty} t^l \psi(t) dt = 0, \quad \text{for} \quad l = 0, 1, 2, \ldots, L - 1 \qquad (12)$$

where L refers to as the moment order. Combining above equations together and further let $L = 2$, we could finally obtain a finite set of coefficients, which is known as the 4-coefficient Daubechies wavelet.

$$c_0 = \frac{1 + \sqrt{3}}{4\sqrt{2}}, \quad c_2 = \frac{3 + \sqrt{3}}{4\sqrt{2}}, \quad c_3 = \frac{3 - \sqrt{3}}{4\sqrt{2}}, \quad c_4 = \frac{1 - \sqrt{3}}{4\sqrt{2}}$$

with all other $c_k = 0$. By using the following iteration process, then the scaling function $\phi_n(t)$ will converge to a continuous function supported on $[0, 2L - 1]$, which has also been plotted in Figure 5 for both $L = 2$ and $L = 4$.

$$\phi_n(t) = \sum_{k \in Z} c_k \sqrt{2} \phi_{n-1}(2t - k) \qquad (13)$$

where the initial scaling function is defined as a indicator function on $[0, 1]$.

$$\phi_0(t) = \begin{cases} 1, & t \in [0, 1] \\ 0, & \text{others} \end{cases} \qquad (14)$$

Given the reconstruction property, we may conveniently expand the MAR signal $g(t)$ into wavelet series [49]:

$$g(t) = w_0^0 + \sum_{n=0}^{\infty} \sum_{k=0}^{2^n-1} w_n^k \psi_{n,k}(t) \tag{15}$$

by properly defining the periodic wavelet $\psi_{n,k}(t)$ according to

$$\psi_{n,k}(t) = \sum_{j \in Z} 2^{n/2} \psi(2^n(t+j) - k) \tag{16}$$

Here, 2^n is the shrunk factor. The wavelet coefficients in (15) can be given by

$$w_0^0 = \int_0^1 g(t)dt, \quad w_n^k = \int_0^1 g(t)\psi_{n,k}(t)dt$$

4.2.3. Why Daubechies Wavelet

Except for the sharing merits of orthogonality, compact support and the presence of amplitude variation under signal discontinuity, short wavelets often seems to be much more effective than long ones in detecting signal ruptures [47]. In practice, the shapes of discontinuities that can be identified by the smallest wavelets are usually simpler than those by the longer wavelets. Although Haar wavelets may have a smaller support, the appealing moment vanishing property, which is of particular interest to discontinuity detection [49], makes the Daubechies wavelets much more competitive in the context of our cluster identification.

Usually, the higher order of a Daubechies wavelet is, the more of its moments are zeros. Specifically, a Daubechies wavelet of an order $2L$ is defined by $2L$ nonzero coefficients $\{c_k\}$, has its first L moments equal to zero and is supported on $[0, 2L - 1]$. Generally speaking, the more moments which are zeros, the more wavelet coefficients that are nearly vanishing for smooth functions F [49]. To elaborate this point, suppose $g(k)$ has L-term Taylor expansion about the point $t_k = k2^{-n}$:

$$g(x) = \sum_{j=0}^{L-1} \frac{1}{j!} g^{(j)}(x_k)(x - x_k)^j + \frac{1}{L!} g^{(L)}(t_x)(x - x_k)^L \tag{17}$$

where t_x lies between x and x_k. Assume that $\psi(t)$ is supported on $[-a, a]$ having its first L moments equal to zeros, and $|g^{(L)}(t)|^2$ is bounded by a constant A on $[(k-a)2^{-n}, (k+a)2^{-n}]$. Then, we may have [49]:

$$|w_k^n| \le \frac{A}{\sqrt{L+1/2}L!} \left(\frac{a}{2^n}\right)^{L+1/2} \tag{18}$$

where w_k^n represent of wavelet coefficients of the input signal $g(k)$.

In essence, the above inequality proves that $\psi(t)$ having vanishing moments produces a large number of small wavelet coefficients, i.e., $w_k^n \to 0$. As a consequence, it is possible to capture the most energy of input signals by using a few coefficients, which is much significant to information compression [47]. More importantly, the large magnitudes of Daubechies coefficients are concentrated around the locations of *non-differentiability* points in $g(k)$, while most other coefficients approach zero for the seamless region. This local-transient analysis illustrates one of powerful features of wavelet analysis, which can be properly used to efficiently detect the MAR discontinuities.

4.2.4. Application Considerations

The deterministic part of MAR signal may undergo abrupt changes in the first or second derivative. Accordingly, the first-level and second-level details show the discontinuity most clearly, as the rupture contains high-frequency part. If we were only interested in identifying discontinuity, the 1st order Daubechies wavelet, (i.e., $L = 1$), which is usually abbreviated to '*db1*', would be a more useful wavelet for most analysis. On the other hand, nevertheless, the presence of noise, which is a common situation in signal processing, makes the identification of discontinuities much more complicated. Then, the signal rupture is sometimes visible at the deeper level decompositions [47]. Besides, as an important criterion in selecting wavelets, the *regularity* property can be considered [45]. In our cluster identification application, we choose to use the 2nd order Daubechies wavelet, (i.e., $L = 2$) abbreviated to '*db2*' that is sufficiently regular for analysis.
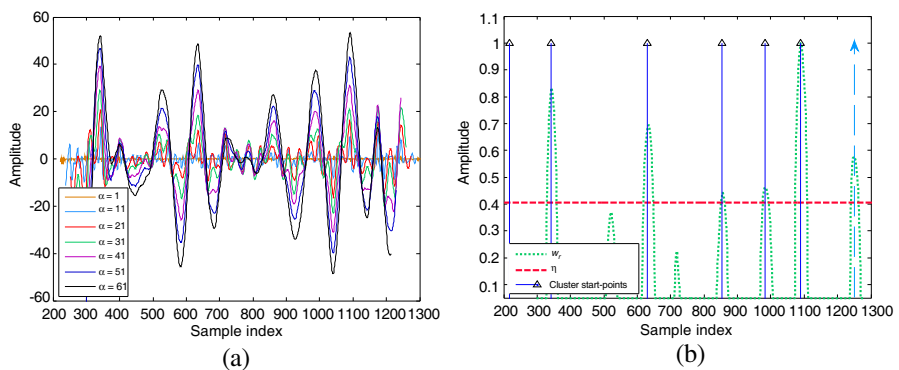

Figure 6. (a) Wavelet coefficients of the MAR signal under different scale values. (b) Wavelet based cluster identification.

In Figure 6(a), we have plotted the derived wavelet coefficients under different scale values α. Two important observations can be made to simulation results. First, the positive local maximum exactly appears in the discontinuity points of MAR signal, indicating the possible clusters breakpoints. Second, with a small scale value, (e.g., $\alpha < 21$), there seems to be a lot of insignificant local maximums which are mainly attributed to the inevitable noise characters, making cluster identification much complicated. Meanwhile, we obviously note from Figure 6(a) that, even if under various different scales, the local maximums of wavelet coefficients are basically *overlapped* with each other. Hence, as expected from (18), the larger scale value can be suggested to facilitate subsequent processing given the moment order L. So, we may use a scale value $\alpha = 51$ in following analysis.

4.2.5. Cluster Extraction

Once the scale value has been determined, we will find local maximums and finally identify cluster breakpoints. Two important things to note in this process is the computational complexity of local maximum searching and the false break-points aroused by noise. To response these two difficulties, furthermore, we present a three-step post-processing algorithm having an efficient computational complexity and is robustness to noise.

Firstly, a *half-wave rectifier* signal of wavelet coefficients is obtained, by setting negative values in $\mathbf{w} = \{w(k), k = 0, 1, \ldots, N - M - 1\}$ to 0, which is denoted by $\mathbf{w}^{\dagger}$. Then, the normalization is performed on $\mathbf{w}^{\dagger}$.

$$\mathbf{w}_r = \mathbf{w}^{\dagger} / \max(\mathbf{w}^{\dagger}) \tag{19}$$

In order to eliminate the false discontinuities, we further set a threshold η which can be used to exclude those insignificant local maximums caused by noise or specula reflections. In practice, there are a lot of threshold selection techniques in existing literatures on noise suppression [47]. Based on our empirical experiment, we may simply set the threshold as (20), and more complex scheme will be considered in the future.

$$\eta = \frac{1 - \mathrm{var}\left(\overline{\mathbf{w}_r|}\right)}{\mathrm{mean}\left(\overline{\mathbf{w}_r|}\right)} \tag{20}$$

where $\overline{\mathbf{w}_r|}$ denotes the subset elements fulfill the condition $w_r(k) > \xi$, where $\xi > 0$ is mainly used to select the dominate wavelet coefficients in $\mathbf{w}_r$. In practice, we may simply set $\xi = 0.1$. And, $\mathrm{var}\,(x)$ and $\mathrm{mean}\,(x)$ give the standard deviation and mean of x, respectively. The derived threshold η has been shown in Figure 6(b). Notice that, two local

maximums locating at 520 and 710 have been excluded. Assume there are I clusters remaining after threshold comparison, we then obtain the range of the ith cluster breakpoint denoted by **ClusterRange**$_i$.

$$\textbf{ClusterRange}_i = \{k \,|\, w_r(k) > \eta, \ k = 0, 1, 2, \ldots, N - M - 1\} \quad (21)$$

Finally, we identify the cluster breakpoint by approximately using

$$\text{ClusterIndex}_i = \text{mean}(\textbf{ClusterRange}_i) \quad (22)$$

Notice that, for one thing, the first breakpoint, (i.e., CIR start-point) can be directly determined, without using the above presented cluster identification. Specifically, we can immediately identify the first breakpoint once the MAR signal $s(k)$ has surpassed a predefined threshold. In practice, this threshold can be conservatively set to 1.5 during experiments, as the summed energy of two successive pieces of signal only containing background noise will basically *equal* each other. For another, although the last cluster breakpoint may exhibit large amplitude, e.g., the cluster located at 1250 in Figure 6(b) which corresponds to the *last* value of **ClusterIndex**, we still exclude it during cluster identification. The main reason is that signal during this range has been greatly attenuated and signal-to-noise ratio (SNR) is rather low, leading to inaccurate cluster identification. Hence, there is the every likelihood that the amplitude change is caused by small-scale fading or noise, rather than a real cluster.

4.3. Algorithm Complexity

Based on the elaborations above, the complete cluster identification algorithm can be depicted as following.

Input: The discrete CIR $h(n)$, the averaging length M, the scale value α.
1. $g(k) = 10 \times \log_{10}\{\sum_{m \in [k, k+M-1]} h^2(m) / \sum_{n \in [k-M, k-1]} h^2(n)\}, \ k = M,$ $M + 1, \ldots, N - M - 1$.
2. $w(k) = \langle g(n), 1/\sqrt{\alpha}\Psi[(n-k)/\alpha]\rangle, \quad n = 0, 1, 2, \ldots, N - M - 1$, and $\langle \mathbf{x}, \mathbf{y} \rangle$ denotes the inner product between $\mathbf{x}$ and $\mathbf{y}$. Fast wavelet transform can be adopted when calculating $w(k)$.
3. $\mathbf{w}_r = \mathbf{w}^\dagger / \max(\mathbf{w}^\dagger)$, and $\mathbf{w}^\dagger = \{w(k) \,|\, w(k) > 0, \ k = 0, 1, 2, \ldots, N - M -1\}$.
4. $\eta = (1 - \text{var}(\mathbf{w}_s))/\text{mean}(\mathbf{w}_s)$, and $\mathbf{w}_s = \{w_s(k) \,|\, w_r(k) > \xi, \ k = 0, 1, 2, \ldots, N - M - 1\}$.
5. **ClusterRange**$_i = \{k \,|\, w_r(k) > \eta, \ k = 0, 1, 2, \ldots, N - M - 1\}$, and then obtain ClusterIndex$_i = \text{mean}(\textbf{ClusterRange}_i)$.

Now, we may analysis the computation complexity of the presented algorithm. The algorithm complexity can be generally

evaluated by the total number of involved multiplication (or division) operations. For the MAR calculation, we need $(N - 2M)$ times of multiplications. Then, during wavelet transform process we only employ $N \log_2 N$ times multiplications when fast wavelet transform (FWT) algorithm is adopted [49]. Finally, for the three-step post-processing algorithm mainly relying upon comparison operations, it is seen that there only need N times multiplications. So, without exhaustive search process the complexity of our presented algorithm can be approached by $O(N \log_2 N + 2N)$, which is computationally efficient for realistic UWB clusters identification. In comparison, based on a trial-fitting mechanics, the linear regression based technique may have an intensive computation complexity of an *exponent* order [17]. Even for the modified method [17, 18], the complexity is still highly complicated, which can be hardly applied to a large amount data analysis.

4.4. Robustness Analysis

We firstly investigate the influence coming from the average length M. In Figure 7(a), we have plotted the derived wavelet coefficients of MAR signal with different M. It can be noted that, within the provided parameter range, i.e., $25 < M < 85$, these wavelet coefficients are basically similar to each other, especially the first five (or six) maximum coefficients which are located at potential cluster start-points. Correspondingly, the identified clusters are shown in Figure 7(b). We can observe that the 3rd and 4th clusters are essentially maintained constant under different M. Nevertheless, we
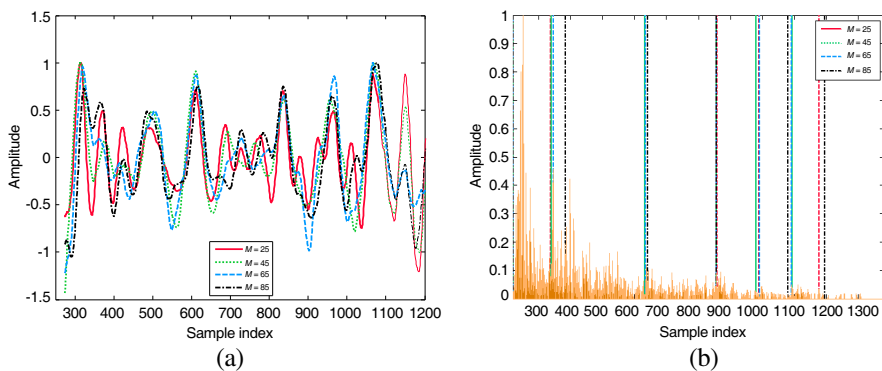

Figure 7. Effects from averaging length M. (a) Wavelet coefficients under different M. (b) Cluster identification results under different M. Notice that, in this experiment, the scale value α is set to 51.
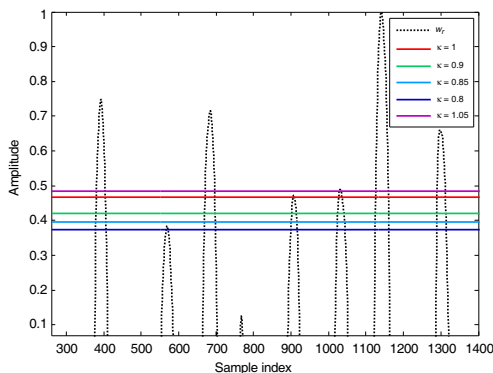
Figure 8. Disturbance analysis of the suggested threshold scheme.

have also noted that, for a much small M, (e.g., $M = 25$), the last cluster may be misinterpreted due to insufficient suppression of the small-scale fading effect. As the cluster identification mainly concentrates on the *former* clusters which are of significance to channel modeling and practical designing, however, the average length of 25 is still practically feasible. On the other hand, for the case of $M = 85$, the identified clusters may deviate noticeably from the exact start-points using a fair M, (e.g., the 2nd cluster). This is mainly attributed to that a large average length may deteriorate the amplitude discontinuity of CIR to some extent. In practice, the maximum M should also be associated with UWB channel characteristics. We assume the cluster interval are typically ranged in [10 50] ns as is reported [9, 16], M is supposed to remain smaller than a *half* of the minimum value, (i.e., 10 ns), in order to completely preserve CIR amplitude discontinuity. Given the frequency sweeping interval and IDFT length, the maximum average length can be then conservatively set to 65.

Besides, we note that from Figure 6(a) that, for different scale values, (e.g., $31 < \alpha < 51$), the derived wavelet coefficients are simply amplified with a larger α, while the relative amplitude of local maximums (especially of the first five maximum coefficients) generally remains unchanged, resulting in the consistent cluster identifications. Hence, in practice the scale value α may have slight influence upon the clustering result.

We have established a simple threshold selection scheme in this research. In order to validate the robustness of our derived threshold, we further introduce a *disturbance* factor κ to address realistic effects, (e.g., noise) on this threshold. That is, we may use $\eta' = \kappa \times \eta$ as a real threshold in practice, and see how this deviation affects

the finally identified clusters. In Figure 8, we have illustrated the different values of κ accompanying the resulting threshold η'. It can be noted that, when $\kappa \in [0.85\ 1]$, the clustering results will essentially remain the same. Nevertheless, a much lower derivation factor, (e.g., $\kappa = 0.8$) will misinterpret the fake cluster located at 570, while a much higher derivation factor, (e.g., $\kappa = 1.05$) may exclude the possible cluster located at 906. Hence, although the relative robustness of such a presented threshold selection, other complicated methods such as adaptive thresholding can be investigated in future research, in order to maintain this cluster identification in good operation even in imperfect conditions.

5. EXPERIMENTAL SIMULATIONS

In this section, the presented cluster identification algorithm will be tested on both simulated UWB CIRs and the measured CIRs in realistic vehicle cabin. In all the following experiments, we set $M = 50$ and $\alpha = 51$.

5.1. Simulated UWB CIRs

We firstly evaluate our suggested algorithm on simulated UWB CIRs, which are generated by using the IEEE 802.15.4a channel modeling. In our simulations, the channel type is CM5, with a predefined cluster arrival rate of 0.0488, that is, the average cluster interval is about 22.32 ns [12]. The derived cluster identification results based on our present algorithm have been shown in Figure 9. We may clearly observe that, when the intercluster signal power follows an exponential decay rule as in simulated CIRs, our algorithm can accurately discover cluster start points in a completely automatic fashion. Meanwhile, even for the non-exponential decay case illustrated in Figure 9(b), (e.g., in NLOS environments), accurate cluster identification can be still guaranteed. The estimated cluster interval, based on independent 50 realizations, is about 23 ns. Therefore, it can be concluded that this new method can indeed efficiently identify multiple clusters in simulated UWB CIRs.

5.2. Measured UWB CIRs

From the extracted UWB CIR shown in Figure 10(b), we may note that, in vehicle cabin environments the PDP does *not* exactly follow an exponent function due to complicated reflections, (e.g., the NLOS case). It is apparent that linear regression based cluster extraction may become totally invalid in this case [17]. On the other hand,
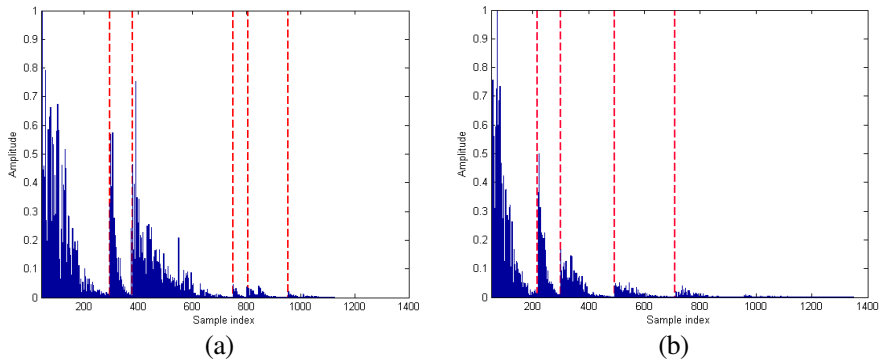
Figure 9. Cluster identification realizations for the IEEE 802.15.4a channel modeling. The cluster arrival interval in CIR generation program is defined to 22.32 ns, and the estimated value based on 50 independent realizations is about 24 ns. (a) The LOS case; and (b) the NLOS case. Notice that, for the NLOS case, the first and third cluster may not exactly follow an exponential decay rule.
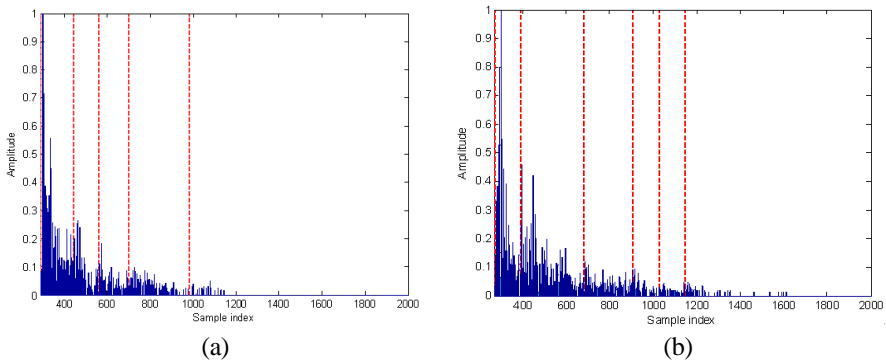

Figure 10. Cluster identification realizations for the measured UWB propagations. (a) The LOS case (Tx3-Rx1); and (b) the NLOS case (Tx3-Rx6).

the sparseness of measured CIRs seems not to be obvious. Hence, HMM inspired technique may either become computationally complex or even fail to produce right clustering results [37]. Nevertheless, independent of any PDP and sparseness characteristic, our proposed method can in essence efficiently identify cluster breakpoints in measured data based on the discontinuity detection mechanic. UWB CIR measurements under different operation conditions have been shown in Figures 10(a) and (b), accompanying the derived cluster

extraction result. From experimental results, it can be clearly seen that, no matter what the operation environment is, (i.e., LOS or NLOS), the suggested technique can automatically identify multiple clusters involved in measurements without any a priori information. As a consequence, this algorithm can be applied to analysis a large amount of measurements in a completely automatic and efficient fashion, which hence allows more comprehensive investigations to UWB propagations [16, 17]. Through the visual inspection, it is naturally to observe the appearance of clusters in the neighborhood of CIR peaks [37], which also keeps identical with the produced cluster identification results, as is illustrated by Figures 9 and 10. Although the reasonable cluster identification results in NLOS case from the most experiments, it is noteworthy that the algorithm may sometimes misinterpret the first couple of clusters due to the adopted simple threshold scheme. Hence, the research on cluster extraction in NLOS cases still remains as an open area in the future.

It should also be emphasized that the identified cluster is basically independent of parameter configurations. The total clusters number contained in measured UWB CIRs is about 5–6 for vehicle environment. The local amplitude discontinuity based cluster identification indeed captures the nature of UWB propagations, and hence is robust to parameter configurations, which is much superior to linear regression based scheme whose clustering result is closed related with specific parameter settings, (i.e., the MSE threshold) [17].

Based on the identification results, we can conveniently derive the cluster arrival interval. From the measured channel CIRs, for the LOS case, the average samples interval between two adjacent clusters, obtained from 20 independent channel realizations, is about 239. Then, given a frequency sweeping step of 1.55 MHz and zero-padded IDFT length of 7724, the estimated cluster arrival interval is about 20.04 ns. Notice that, this estimated cluster arrival interval in vehicle environments is much different from the 802.15.3a channel modeling, in which the typical value is about 42.91 ns. In fact, clusters arrival is closely associated with specific operation environments. For the IEEE 802.15.3a channel modeling, the parameters are essentially extracted from *indoor* measurements [9, 11], in which the distance between significant objects, (i.e., walls) is much larger than that of in a vehicle cabin. And correspondingly, in indoor applications the runtime between these objects to receiver is also much larger than in a small vehicle cabin, leading to a quite different cluster arrival character. On the other hand, it is noted that, for the more general 802.15.4a channel modeling, (e.g., CM5), this obtained result essentially agrees with the typically specified value of 22 ns. For the NLOS condition,

the average sample interval is about 174, and the corresponding cluster arrival interval is about 14.53 ns. Compared with the specified value in current standards, this estimated cluster arrival interval also basically matches the typical value of 14.99 ns [12].

6. CONCLUSIONS

We have presented a novel cluster identification algorithm in this paper. Rather than by resorting to power decay characteristics, our method is premised on the local amplitude discontinuity generally introduced by different clusters. To reinforce the cluster breakpoints, MAR transform is firstly performed on UWB CIRs. By exploiting the powerful local-transient analysis ability of CWT, we then developed a computationally efficient cluster extraction scheme. Even if the current state-of-the-art linear-regression method fails to identify cluster due to complex realistic propagations, (e.g., non-exponential PDP), our algorithm can still produce satisfactory clustering results which also keeps identical with visual inspections. This algorithm is robust to parameter configurations, which essentially relies upon realistic physical propagations. Meanwhile, by excluding the interactive process, the algorithm can automatically identify clusters in UWB CIRs, which is hence significant to the larger amount of measurement processing. Experiments on the measured data in a vehicle cabin as well as the simulated CIRs validate our proposed method. The estimated cluster arrival parameter, derived from the clustering results, is also comprehensively analyzed. Generally, this algorithm provides a compelling framework for cluster identification during channel modeling, which allows the more profound understanding to realistic UWB propagations. Aiming to further improve the clustering accuracy, especially in the NLOS environments, our future investigations may focus on the adaptive wavelet analysis based cluster identification.

REFERENCES

1. Yang, L. Q. and G. B. Giannakis, "Ultra-wideband communications: An idea whose time has come," *IEEE Signal Proc. Mag.*, Vol. 21, No. 6, 26–54, 2004.

2. Withington, P., H. Fluhler, and S. Nag, "Enhancing homeland security with advanced UWB sensors," *IEEE Microw. Mag.*, Vol. 4, No. 3, 51–58, 2003.

3. Cheolhee, P. and T. S. Rappaport, "Short-range wireless communications for next-generation networks: UWB, 60 GHz millimeter-wave WPAN, and ZigBee," *IEEE Wirel. Commun.*, Vol. 14, No. 4, 70–78, 2007.

4. Alomainy, A., A. Sani, A. Rahman, J. Santas, and Y. Hao, "Transient characteristics of wearable antennas and radio propagation channels for ultra-wideband body-centric wireless communications," *IEEE Trans. Antennas Propag.*, Vol. 57, No. 4, 875–884, Apr. 2009.

5. Win, M. Z. and R. A. Scholtz, "Ultra-wide bandwidth time hopping spread spectrum impulse radio for wireless multiple-access communications," *IEEE Trans. on Commun.*, Vol. 48, No. 4, 679–689, 2000.

6. Batra, A., J. Balakrishnan, G. R. Aiello, J. R. Foerster, and A. Dabak, "Design of a multiband OFDM system for realistic UWB channel environments," *IEEE Trans. Microwave Theory Tech.*, Vol. 52, No. 9, 2123–2138, Sep. 2004.

7. Cramer, R. J., R. A. Scholtz, and M. Z. Win, "Evaluation of an ultra-wideband propagation channel," *IEEE Trans. Antennas Propag.*, Vol. 50, No. 5, 561–570, May 2002.

8. Cassioli, D., M. Z. Win, and A. F. Molisch, "The ultra-wide bandwidth indoor model: From statistical model to simulations," *IEEE J. Select. Areas Commun.*, Vol. 20, No. 9, 1247–1257, 2002.

9. Molisch, A. F., K. Balakrishnan, C. C. Chong, D. Cassioli, S. Emami, A. Fort, J. Karedal, J. Kunisch, H. Schantz, K. Siwiak, and M. Z. Win, "A comprehensive model for ultra-wideband propagation channels," *IEEE Trans. Antennas Propag.*, 3151–3166, 2006.

10. Saleh, A. and R. Valenzuela, "A statistical model for indoor multipath propagation," *IEEE J. Select. Areas Commun.*, Vol. 5, No. 2, 128–137, Feb. 1987.

11. Foerster, J. (ed.), "IEEE 802.15.SG3a channel modeling sub-committee report final," *IEEE p802.15-02/490r1-SG3a*, Feb. 2003.

12. Molisch, A. F., et al., "IEEE 802.15.4a channel model — Final report," *IEEE 802.15-04-0662-00-004a*, Nov. 2004.

13. Carbonelli, C. and U. Mitra, "Clustered ML channel estimation for ultra-wideband signals," *IEEE Trans. Wirel. Commun.*, Vol. 6, No. 7, 2412–2416, 2007.

14. Witrisal, K., G. Leus, G. Janssen, M. Pausini, F. Troesch, T. Zasowski, and J. Romme, "Noncoherent ultra-wideband systems," *IEEE Signal Proc. Mag.*, Vol. 26, No. 4, 48–66, 2009.

15. Chen, Z. and Y.-P. Zhang, "Effects of antennas and propagation channels on synchronization performance of a pulse-based ultra-wideband radio system," *Progress In Electromagnetics Research*, Vol. 115, 95–112, 2011.

16. Molisch, A. F., "Ultra-wideband propagation channels," *IEEE Proc.*, Vol. 97, No. 2, 353–371, Feb. 2009.

17. Chuang, J., S. Bashir, and D. G. Michelson. "Automated identification of clusters in UWB channel impulse responses," *Proc. of Canadian Conference on Electrical and Computer Engineering (CCECE)*, 761–764, 2007.

18. Stefanski, A., "Characterization of radio-wave propagation in indoor industrial environments," Degree Thesis, Simon Fraser University, 2010.

19. Ciccognani, W., A. Durantini, and D. Cassioli, "Time domain propagation measurements of the UWB indoor channel using PN sequence in the FCC-compliant band 3.6–6 GHz," *IEEE Trans. Antennas Propag.*, Vol. 53, No. 4, 1542–1549, Apr. 2005.

20. Haneda, K., J.-I. Takada, and T. Kobayashi, "Cluster properties investigated from a series of ultra-wideband double directional propagation measurements in home environments," *IEEE Trans. Antennas Propag.*, Vol. 54, No. 12, 3778–3788, 2006.

21. Nikookar, H. and R. Prasad, *Introduction to Ultra Wideband for Wireless Communications, Signals and Communication Technology*, 164–171, Springer Science & Business Media B.V., Berlin, 2009.

22. Li, X., L. Yang, S. X. Gong, and Y. J. Yang, "A novel tri-band-notched monopole antenna," *Journal of Electromagnetic Waves and Applications*, Vol. 23, No. 1, 139–147, 2009.

23. Song, H. W., J. N. Lee, J. K. Park, and H.-S. Lee, "Design of ultra wideband monopole antenna using parasitic open loops," *Journal of Electromagnetic Waves and Applications*, Vol. 23, No. 5–6, 561–570, 2009.

24. Danesfahani, R., L. Asadpor, and S. Soltani, "A small UWB

CPW-FED monopole antenna with variable notched bandwidth,"
Journal of Electromagnetic Waves and Applications, Vol. 23,
No. 8–9, 1067–1076, 2009.

25. Chen, D. and C. H. Cheng, "A novel compact ultra-
wideband (UWB) wide slot antenna with via holes," *Progress In
Electromagnetics Research*, Vol. 94, 343–349, 2009.

26. De Villiers, J. P. and J. P. Jacobs, "Gaussian process modeling of
CPW-FED slot antennas," *Progress In Electromagnetics Research*,
Vol. 98, 233–249, 2009.

27. Hu, S., C. L. Law, and W. B. Dou, "A tapered slot antenna with
flat and high gain for ultra-wideband applications," *Journal of
Electromagnetic Waves and Applications*, Vol. 23, No. 5–6, 723–
728, 2009.

28. Gao, G. P., M. Li, S. F. Niu, X. J. Li, B. N. Li, and J. S. Zhang,
"Study of a novel wideband circular slot antenna having frequency
band-notched function," *Progress In Electromagnetics Research*,
Vol. 96, 141–154, 2009.

29. Xia, Y. Q., J. Luo, and D. J. Edwards, "Novel miniature printed
monopole antenna with dual tunable band-notched characteristics
for UWB applications," *Journal of Electromagnetic Waves and
Applications*, Vol. 24, No. 13, 1783–1793, 2010.

30. Gong, J.-G., Q. Li, G. Zhao, Y. Song, and Y.-C. Jiao, "Design
and analysis of a printed UWB antenna with multiple band-
notched characteristics," *Journal of Electromagnetic Waves and
Applications*, Vol. 23, No. 13, 1745–1754, 2009.

31. Lin, C. C. and H. R. Chuang, "A 3–12 GHz UWB planar
triangular monopole antenna with ridged ground-plane," *Progress
In Electromagnetics Research*, Vol. 83, 307–321, 2008.

32. Wang, J. J., Y. Z. Yin, and X. W. Dai, "A novel fractal triangular
monopole antenna with notched and truncated ground for UWB
application," *Journal of Electromagnetic Waves and Applications*,
Vol. 23, No. 10, 1313–1321, 2009.

33. Eldek, A. A., "Numerical analysis of a small ultra-wideband
microstrip-FED tap monopole antenna," *Progress In Electromag-
netics Research*, Vol. 65, 59–69, 2006.

34. Bose, R., B. D. Steinberg, and A. Freedman, "Sequence
CLEAN: A deconvolution technique for reducing side-lobe
artifacts in microwave images of continuous targets," *Proc. of
the Thirteenth Annual Benjamin Franklin Symposium on Antenna
and Microwave Technology in the 1990s*, May 1995.

35. Alsehaili, M., S. Noghanian, A. R. Sebak, and D. A. Buchanan,

"Angle and time of arrival statistics of a three-dimensional geometrical scattering channel model for indoor and outer propagation environment," *Progress In Electromagnetics Research*, Vol. 109, 191–209, 2010.

36. Fuhl, J., J. P. Rossi, and E. Bonek, "High-resolution 3D direction-of-arrival determination for urban mobile radio," *IEEE Trans. Antennas Propag.*, Vol. 45, 672–682, Apr. 1997.

37. Shutin, D. and G. Kubin. "Cluster analysis of wireless channel impulse responses with hidden markov models," *Proc. of IEEE International Conference on Acoustics, Speech, and Signal Processing (ICASSP)*, 949–952, May 2004.

38. Erceg, V., et al., "TGn channel models," *IEEE 802.11-03/940r4*, May 2004.

39. Proakis, J. G., *Digital Communications*, 4th edition, McGraw-Hill Companies, Inc., New York, USA, 2001.

40. Canny, J., "A computational approach to edge detection," *IEEE Trans. Pattern Anal. Mach. Intell.*, Vol. 8, 679–698, 1986.

41. Zhang, L. and P. Bao, "Edge detection by scale multiplication in wavelet domain," *Pattern Recogn. Lett.*, Vol. 23, No. 14, 771–1784, 2002.

42. Heric, D. and D. Zazula, "Combined edge detection using wavelet transform and signal registration," *Image Vision Comput.*, Vol. 25, No. 5, 652–662, May 2007.

43. Lazaro, A., D. Girbau, and R. Villarino, "Wavelet-based breast tumor location technique using a UWB radar," *Progress In Electromagnetics Research*, Vol. 98, 75–95, 2009.

44. Gijbels, I., A. Lambert, and P. Qiu, "Edge-preserving image denoising and estimation of discontinuous surfaces," *IEEE Trans. Pattern Anal. Mach. Intell.*, Vol. 28, No. 7, 1075–1087, Jul. 2006.

45. Daubechies, I., *Ten Lectures on Wavelets*, SIAM, 1992.

46. Hernandez, E. and G. Weiss, *A first Course on Wavelets*, CRC Press, 1996.

47. Coifman, R. and M. V. Wickerhauser, "Wavelets and adapted waveform analysis," *Mathematics and Applications*, J. Benedetto and M. Frazier (eds.), CRC Press, Wavelets, 1994.

48. Mallat, S. G., "A theory of multi-resolution signal decomposition: the wavelet representation," *IEEE Trans. Pattern Anal. Mach. Intell.*, Vol. 11, 674–693, 1989.

49. Walker, J. S., "Fourier analysis and wavelet analysis," *Notices of the American Mathematical Society*, Vol. 44, No. 6, 658–670, 1997.